



Cite this: *Chem. Sci.*, 2025, **16**, 22611

All publication charges for this article have been paid for by the Royal Society of Chemistry

Received 26th July 2025  
Accepted 18th October 2025

DOI: 10.1039/d5sc05604g  
[rsc.li/chemical-science](http://rsc.li/chemical-science)

## Introduction

Optical tweezers have been utilized in a wide range of applications, including the isolation of molecules in the gas phase or the manipulation of living cells by using the confocal laser.<sup>1–7</sup> In the current manipulation technique, both the diffraction limit and the limited laser power restrict the accessible target range to a sub-micron scale.<sup>8,9</sup> Despite this fact, recent theoretical and experimental approaches have demonstrated that molecular manipulation at metal interfaces under plasmon resonance conditions could be a breakthrough for addressing these inherent limitations.<sup>10–12</sup> Recent studies indicate that, in contrast to traditional optical trapping methods, plasmon-driven molecular manipulations exhibit distinctive features originating from the intrinsic properties of plasmon resonance, including local heating, the transfer of hot electrons, or a nonlinear response to propagating light.<sup>13–19</sup> In plasmonic molecular trapping, various factors, such as an optical pressure

from the enhanced electromagnetic field, a localized thermal elevation, interfacial chemical reactions, and intermolecular interactions, have been proposed as mechanisms.<sup>20,21</sup> However, the thermophoresis effects induced by plasmonic heating and optical forces acting on non-resonant targets with approximately 10 nm in size are typically inadequate for retaining molecules within the hotspot.<sup>11,22,23</sup> Thus, many aspects of plasmon-assisted molecular trapping, especially those related to the adsorption and diffusion of individual molecules, remain unexamined.

We recently demonstrated that organic molecules, approximately 1 nm in size, can be condensed within the plasmon-enhanced electric field at the interface between water and metal at ambient temperature. This phenomenon occurs despite the fact that the local optical force on non-resonant molecules is weaker than the force required to trap individual molecules within the hotspot.<sup>11,24,25</sup> This fact suggests that intermolecular interactions play a critical role in determining the optical potential, facilitating efficient molecular condensations.<sup>26,27</sup> Moreover, it is essential to emphasize that the strongest optical trapping force was found to act on 44bpy molecules with a distinct molecular configuration, which has a distinct polarizability in response to an optical field. We found that plasmonic manipulation can induce highly packed molecular domains that are unattainable under conventional optical trapping conditions. However, the underlying factors governing

Department of Chemistry, Faculty of Science, Hokkaido University, Sapporo, Hokkaido 060-0810, Japan. E-mail: [kei@sci.hokudai.ac.jp](mailto:kei@sci.hokudai.ac.jp)

† Present address: Institute of Physics, École Polytechnique Fédérale de Lausanne (EPFL), Lausanne, CH-1015, Switzerland.

‡ Present address: Department of Chemical Science and Engineering, Graduate School of Engineering, Kobe University, Rokkodai-cho 1-1, Nada-ku, Kobe, 657-850, Japan.



molecular condensations, such as dynamic solvation interactions with solvent molecules and the physicochemical behavior of adsorbates at metal interfaces, are yet to be fully elucidated.

From such backgrounds, this study elucidated key physicochemical parameters that govern plasmon-driven molecular condensation at metal interfaces under ambient conditions through SERS measurements, which offer enhancement factors of the Raman signal up to  $10^8$  *via* both electromagnetic and chemical mechanisms.<sup>13,28–30</sup> Specifically, we revealed how solvent species and the presence of co-adsorbed ions critically influence the adsorption equilibrium and two-dimensional (2D) diffusion of physisorbed molecules in the plasmonic field.<sup>31–33</sup> For the investigation of the molecular interactions involving solvents or ion pairing, we have utilized five different solvents, with and without the electrolyte. Systematic variations of each solvent environment revealed that water uniquely facilitates molecular condensations beyond thermal equilibrium, owing to its reduced solvation energy and suppressed thermal diffusion, because of its high molarity and thermal conductivity.<sup>11,27</sup> Furthermore, we identified that cation–π interactions play a central role in stabilizing localized adsorption domains, where the tuning of ionic concentration enabled control over intermolecular electrostatic interactions. These static forces synergistically act with the plasmon-induced optical force to cooperatively form highly ordered molecular condensed phases.

Our findings thus establish solvent selection and ion concentration as decisive parameters for engineering molecular trapping at plasmonic interfaces, offering a new platform for dynamic and spatially resolved chemical control in nanoscience.

## Results and discussion

### Vibrational features of adsorbed 44bpy in each solvent probed by SERS

The Au nanoprisms array substrates prepared using the template method exhibited a resonance wavelength of approximately 780 nm, which led to SERS enhancement under 785 nm laser illumination (see Fig. SI-1).<sup>26,34,35</sup> Using this substrate, we performed SERS measurements of  $1 \text{ mmol L}^{-1}$  4,4'-bipyridine (44bpy) in various solvents: ultrapure  $\text{H}_2\text{O}$ , *N,N'*-dimethylformamide (DMF), acetonitrile (AN), isopropanol (IPA), and *n*-hexane (Hex). Under the present experimental conditions, approximately 100 nanoprism dimers were present within the laser spot with a spot diameter of around  $3 \mu\text{m}$ . It is important to note that, due to the similar refractive index values for all solvents, the wavelength of plasmon resonance may exhibit independence on solvents. Also, we carefully considered the plasmon modulation by solvent, known as chemical damping, but we concluded that its effect could be ignored

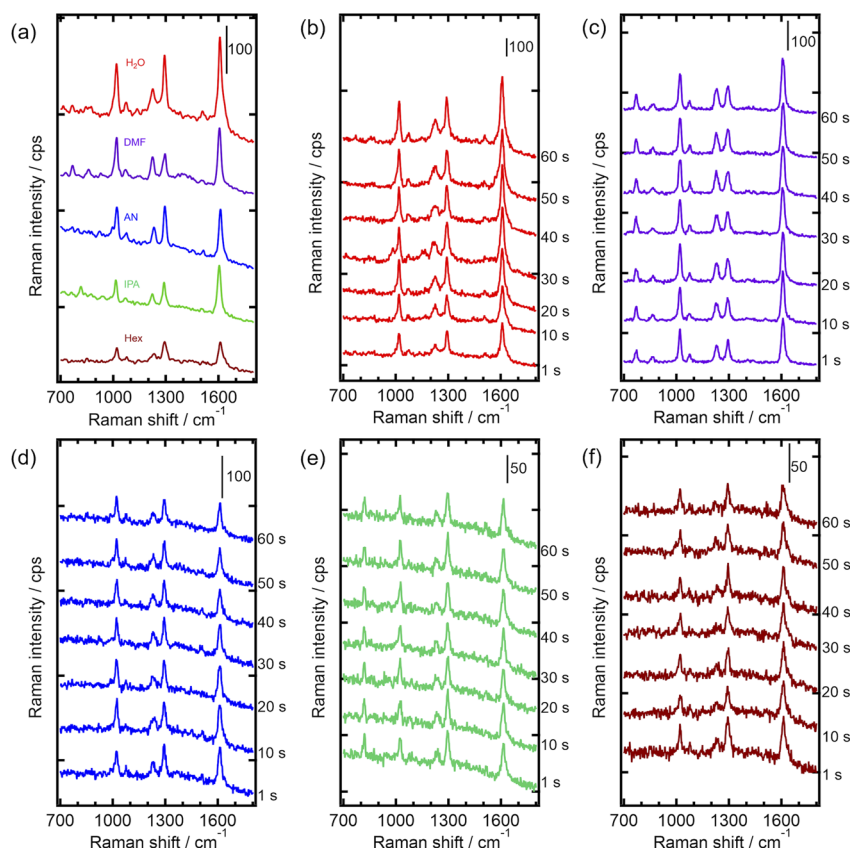


**Fig. 1** SERS spectra of  $1 \text{ mmol L}^{-1}$  44bpy in various solvents with a Au dimer nanoprisms array. All spectra are obtained with 1 s under a  $140 \mu\text{W} \mu\text{m}^{-2}$  laser at room temperature. (a) The spectra of each solution at initial illumination are indicated in red, purple, blue, green, and brown, corresponding to  $\text{H}_2\text{O}$ , DMF, AN, IPA, and Hex, respectively. (b–f) Time-series SERS spectra under 60 s continuous illumination are obtained in each solution with different solvents: (b)  $\text{H}_2\text{O}$ , (c) DMF, (d) AN, (e) IPA, and (f) Hex.



based on the deviation of the plasmon background in SERS (discussed in Fig. SI-2).<sup>36</sup> Fig. 1a shows SERS spectra of 44bpy adsorbed on the Au nanoprisms array immersed in each solvent. Note that no spectrum of 44bpy was obtained when the focus was defocused from the interface. The vibrational modes at 1020, 1223, 1293, and 1610  $\text{cm}^{-1}$  were assigned to the ring breathing, the C–H in-plane deformation, the C–C inter-ring stretching, and C–C/C–N ring stretching, respectively.<sup>37</sup> The oscillating vertical electric field at the metal interface, induced by plasmon resonance, enables to enhance SERS scattering intensities to reveal the molecular adsorption orientation. When the peak intensity ratio of C–C inter-ring stretching at 1293  $\text{cm}^{-1}$  to C–H in-plane deformation at 1223  $\text{cm}^{-1}$  exceeds 1.5, the adsorbed 44bpy shows a vertical orientation with a single N atom attached to the Au surface, referred as the stand-up orientation.<sup>26,32,38</sup> Thus, the spectra of 44bpy in  $\text{H}_2\text{O}$ , AN, IPA, and Hex show nearly identical spectral shapes, indicating a consistent adsorbed orientation against the Au surface. On the other hand, in DMF, the intensity ratio of C–C inter-ring stretching at 1293  $\text{cm}^{-1}$  to C–H in-plane deformation at 1223  $\text{cm}^{-1}$  was relatively smaller, indicating more tilted orientations *via* dipole modulations by anisotropic solvation of DMF (the correlation plots are provided in Fig. SI-3a and b).<sup>37,38</sup> Importantly, variations in the Raman intensities of molecules were observed depending on the solvent species. The signal intensity in  $\text{H}_2\text{O}$  was the highest, while that in Hex was the lowest. Since the molecular Raman signal originates from the surface species on Au, these differences clearly show that the average number of molecules undergoing surface diffusion at the hot spots varies with the choice of solvent.<sup>39</sup>

Time-series changes in SERS intensity are shown from the bottom to the top in Fig. 1b–f. All SERS spectra of 44bpy adsorbed on Au exhibited consistent Raman features over time. Notably, in the case of  $\text{H}_2\text{O}$ , the SERS intensity exhibited a nearly monotonic increase from 1 to 60 seconds. In contrast, the scattering intensities in other solvents remained relatively constant over the same time frame. Note that, due to the non-uniformity of the Au nanoprisms prepared by the template method, the SERS intensity was dependent on the observation sites even under identical optical set-up conditions. To prevent the structure dependences, we recorded averaged Raman intensities over more than five different sites. From this, a consistent evaluation of solvent-dependent tendencies became possible. Essentially, the scattering intensity reflects the number of target molecules at the observation site. The observed increase in  $\text{H}_2\text{O}$  suggests a gradual accumulation of molecules within the plasmonic field, resulting from two-dimensional diffusion under continuous illumination. This gradual increase in the total number of molecules has also been observed and discussed in our previous reports.<sup>11,38</sup> Notably, the SERS spectral shapes and the peak positions remained unchanged during continuous illumination in every solvent (further discussion in Fig. SI-3c and d), confirming that the adsorption orientation was stable throughout measurements. Considering the molecular orientation, a key factor in determining the anisotropic molecular polarizability tensor and, consequently, the optical gradient force, helps to elucidate the

observed solvent dependence. In our measurements, the stand-up orientation of 44bpy in  $\text{H}_2\text{O}$  feels a greater optical trapping force compared to the more tilted configuration observed in DMF, likely due to anisotropic solvation effects. Together with the intensity variations shown in Fig. 1, this result indicates that the solvent dictates not only the preferred adsorption geometry but also the rate of 2D diffusions. Although further quantitative investigation is warranted, these results imply that the choice of solvent affects the optical force exerted on adsorbates at the metal interface. It should also be noted that, although some organic solvents are highly volatile, the solution volume in the cell remained essentially unchanged after SERS measurements, indicating a quasi-steady state. Thus, the volatilization of the solvent would not affect the analyses.

### Time-resolved plasmon-induced molecular motions in five solvents

In Fig. 2a–e, the average peak intensities at 1610  $\text{cm}^{-1}$  ( $I_t$ ) in each solvent, along with their standard deviations ( $\sigma_t$ ) represented as error bars, are plotted against the laser illumination time. The values are normalized by the Raman intensity ( $\sigma_t/I_t$ ). Among the solvents, only the  $\text{H}_2\text{O}$  solution exhibits an apparent increase in average Raman intensity over time, whereas the intensities in other solvents remain relatively constant (Fig. 2a–d). Based on these average results, the Raman intensity of 44bpy is considered to be closely related to the number of molecules adsorbed in each solvent. As expected from the results in Fig. 1, high intensities were observed in  $\text{H}_2\text{O}$ , DMF, and AN, while low intensities were confirmed in IPA and Hex. While the SERS intensity depends on both the number of adsorbed molecules and the site-specific enhancement, the  $\sigma_t$  mainly reflects the inhomogeneity of SERS enhancement among hotspots. As shown in Fig. 2a–d, the deviation observed at the initial stage of irradiation reflects the magnitude of molecular response fluctuations within the plasmonic field. For most solvents, the initial normalized deviation is approximately 0.5, demonstrating that the nanoprism array substrate provides sufficient homogeneity across different solutions. In contrast,  $\text{H}_2\text{O}$  exhibits a larger value (−0.7). These deviations are influenced by the specific enhancement at the hot spot during the early phase (1–30 seconds), highlighting the interplay between the plasmonic electric field and molecular response. In contrast, the standard deviation in DMF increases over time, suggesting that heat generation and molecular diffusion vary significantly across different sites, an inverse trend compared to that observed in  $\text{H}_2\text{O}$ .

In the case of  $\text{H}_2\text{O}$ , the scattering intensity increased to 1.5 times its initial value in about 50 seconds, while remaining almost constant in other solutions. The molecular condensation of 44bpy could be attributed to a modulated equilibrium of motions associated with Brownian motion, such as lateral hopping and thermal fluctuations at the interface caused by plasmon excitations. Additionally, it can be expected that the outflow of molecules from hotspots would be further accelerated by thermal diffusion, facilitating the movement of molecules away from the hotspot through thermophoresis.<sup>40,41</sup> The



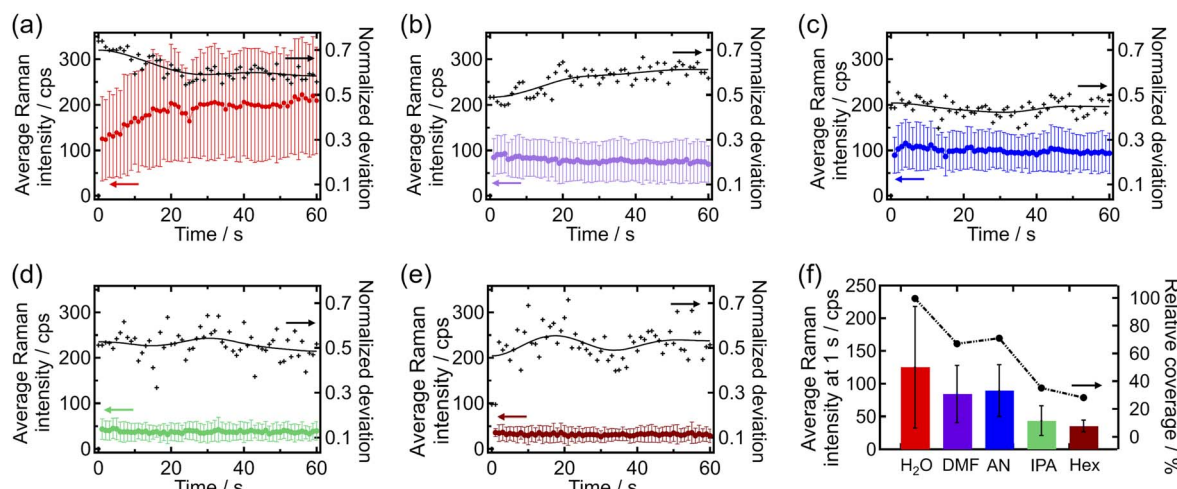


Fig. 2 Average SERS spectral intensities of the vibrational peak at  $1608\text{ cm}^{-1}$  of  $1\text{ mmol L}^{-1}$  44bpy in various solvents with a Au dimer nanoprism array. All original spectra are obtained under  $140\text{ }\mu\text{W }\mu\text{m}^{-2}$  laser power at room temperature. (a–e) Average Raman intensity plots at  $1608\text{ cm}^{-1}$  are plotted as a function of time, which were derived from more than 5 trials for each different solvent. The standard deviation is displayed as colored bars and in the form of normalized deviation plots based on Raman intensity for the right axis with a black fitted line. These plots are colored with red, purple, blue, green, and brown for (a)  $\text{H}_2\text{O}$ , (b) DMF, (c) AN, (d) IPA, and (e) Hex, respectively. (f) The mean intensity at 1 s for each solvent (same color manner as in panels a–e) is summarized together with its standard deviation. Black circles represent the relative surface coverage of 44bpy in each solvent, estimated from the SERS intensities.

similarity in 2D diffusion velocities suggests that the Brownian motion of 44bpy on the Au surface is primarily governed by interfacial conditions, which remain consistent across the solvents due to the identical substrate structure and comparable temperature. However, the thermal diffusion velocity in  $\text{H}_2\text{O}$  is relatively smaller than that in others, as  $\text{H}_2\text{O}$  possesses the highest thermal conductivity. Assuming a local temperature gradient of  $5 \times 10^8\text{ K m}^{-1}$  near a hotspot, the thermal drift velocity of 44bpy in  $\text{H}_2\text{O}$  was estimated to be  $1.3 \times 10^{-3}\text{ m s}^{-1}$  along with the thermal gradient from the plasmon heating spot to solvent, while in DMF, the velocity is calculated to be  $3.0 \times 10^{-3}\text{ m s}^{-1}$  (based on our previous investigation using a similar setup; details of the estimation are provided in SI Section 4). This variation in thermal drift velocity across different solvents appears to play an important role in determining molecular condensation behavior under illumination. The calculated effective thermal potential for the 44bpy molecule along the thermal drift coordinate is  $-0.15\text{ kJ mol}^{-1}$  in  $\text{H}_2\text{O}$ , which is comparable to the estimated plasmon-induced optical potential of  $-0.2\text{ kJ mol}^{-1}$  for 44bpy.<sup>11</sup> On the other hand, the effective thermal potential in other solvents is lower than  $-0.35\text{ kJ mol}^{-1}$ , which exceeds the optical potential and pushes molecules outside.

Based on the above investigations, it was suggested that factors such as surface coverage and 2D diffusion behavior, which depend on the solvent species, are crucial factors that trigger molecular condensation within the plasmonic field. We estimated the relative coverage ( $\theta$ ) from the SERS intensity at the initial state, which corresponds to the adsorption amount of solvated 44bpy on the Au surface from the Temkin model adsorption isotherm as in eqn (1) (Fig. 2f).<sup>31</sup>

$$\frac{\theta}{1-\theta} \exp(-2\alpha\theta) = \exp(-\Delta G^0/RT) \alpha_{\text{sol}} \quad (1)$$

where the standard adsorption free energy  $\Delta G^0$  is defined by the difference in chemical potential between the adsorbed and dissolved state:  $\Delta G^0 = \bar{\mu}_{\text{ads}}^0 - \bar{\mu}_{\text{sol}}^0$ . The constant  $\alpha_{\text{sol}}$  is defined as the ratio of the molar concentrations of 4,4'-bipyridine and the solvent:  $\alpha_{\text{sol}} = c_{\text{44bpy}}/c_{\text{solvent}}$ .  $R$  is the universal gas constant with a value of  $8.314\text{ J mol}^{-1}\text{ K}^{-1}$ .  $T$  corresponds to the solution temperature (298 K). The typical value of  $\Delta G^0$  for 44bpy on Au in water is  $-35.0\text{ kJ mol}^{-1}$ , and the molecular-interaction coefficient  $\alpha$  was estimated to be 1.3 from experimental fitting.<sup>31</sup> From the equation, the  $\theta$  of  $1\text{ mol L}^{-1}$  44bpy on the Au surface in  $\text{H}_2\text{O}$  is estimated to be 99.7%. Based on these isotherms, the  $\theta$  in various solvents can also be roughly estimated as follows: 67% in DMF, 71% in AN, 35% in IPA, and 28% in Hex, as indicated by the SERS intensity difference shown in Fig. 2f. The surface coverage of 44bpy is strongly dependent on solvent species, as the definition of Gibbs energy from the dissolved states to the adsorbed states. This can be attributed to the greater stabilization of 44bpy in organic solvents compared to  $\text{H}_2\text{O}$ , resulting in a smaller Gibbs energy change.<sup>42,43</sup> For example, IPA has the highest solubility or solvation energy for 44bpy, which results in the adsorption of 44bpy being depressed. After 60 seconds of laser illumination in water (Fig. 2a), the estimated surface coverage reached 167% of the equilibrium monolayer value under the simple model. It is noteworthy that the relatively high surface coverage would reduce the intermolecular distance or disorder among well-aligned domain parts, leading to a high density above the expected coverage of the Temkin model. This arises from the different packing structure induced by optical condensation, as generally discussed in the context of optical tweezers.<sup>6,44</sup> It should be noted that this condensed structure at the nanostructured interfaces would result in changes in the solvation and adsorption Gibbs energies from the idealized model *via* the

polariton-induced detuning of molecular states, or localized heat generation.<sup>45–49</sup> In other words, the thermodynamic parameters governing adsorption, such as  $\Delta G^0$  in the Temkin isotherm, may not directly reflect bulk-phase values but represent an optically perturbed interfacial regime.

### Electrolyte-mediated enhancement and suppression of plasmon-induced molecular condensation *via* cation–π interactions

For further understanding of molecular condensation behavior, we investigated the effect of an electrolyte on plasmonic molecular condensation. Based on the thermal diffusion model, the electrolyte concentration modulates the drift velocity and the effective potential on the surface.<sup>23</sup> In the present experiments, we added the supporting electrolyte ( $\text{NaClO}_4$ ) to  $\text{H}_2\text{O}$  and AN with different concentrations. By changing the concentration, the molecular interaction can be tuned through the cation ( $\text{Na}^+$ )–π interaction. In Fig. 3a and b, the ratios of SERS intensity at  $1610\text{ cm}^{-1}$  at a specific laser illumination time against the initial intensity are plotted. Here, the time-dependent SERS intensities were normalized using the initial value at 1 s, and the normalized traces from several measurements were then averaged. Fig. 3a, obtained in  $\text{H}_2\text{O}$ , shows a continuous increment in scattering intensity, corresponding to molecular condensations, during a 60 second laser exposure time across all concentration conditions. On the other hand, for the AN case (Fig. 3b), rapid intensity increments were observed

within the initial 30 seconds in the  $100\text{ mmol L}^{-1}$   $\text{NaClO}_4$  solution, whereas no increments were observed at  $0\text{ mmol L}^{-1}$   $\text{NaClO}_4$ . As discussed above, no condensation behavior was observed in the absence of the electrolyte (Fig. 2) due to the relatively high diffusion velocity associated with the thermal gradient. The dependence of the intensity ratio on the electrolyte concentration is depicted in Fig. 3c. These results confirmed that, in both  $\text{H}_2\text{O}$  and AN cases, distinct condensations could be triggered in the presence of  $100\text{ mmol L}^{-1}$  electrolyte, while the condensation of 44bpy was prohibited at higher concentrations exceeding  $300\text{ mmol L}^{-1}$ . This local maximum cannot be explained by the contribution of thermophoresis, which is monotonously suppressed by electrolyte concentration.<sup>23</sup> Importantly, in  $\text{H}_2\text{O}$ , we found that the addition of electrolytes increased the molecular coverage estimated from the intensity ratio. These results suggest that the molecular aggregation process is influenced not only by the optical modulation of 2D diffusion but also by the intermolecular attraction among adsorbates. This phenomenon is thought to originate from cation binding to 44bpy, which introduces an attractive interaction to the adsorbed molecules. Consequently, it can be inferred that higher electrolyte concentrations above  $100\text{ mmol L}^{-1}$  would lead to the distinct electrical repulsion of the cations, which inhibits condensation.

To verify the interaction of 44bpy and  $\text{NaClO}_4$  in solution, we examined the chemical shift in  $^1\text{H}$  NMR spectra at various electrolyte concentrations. The position of the chemical shift in

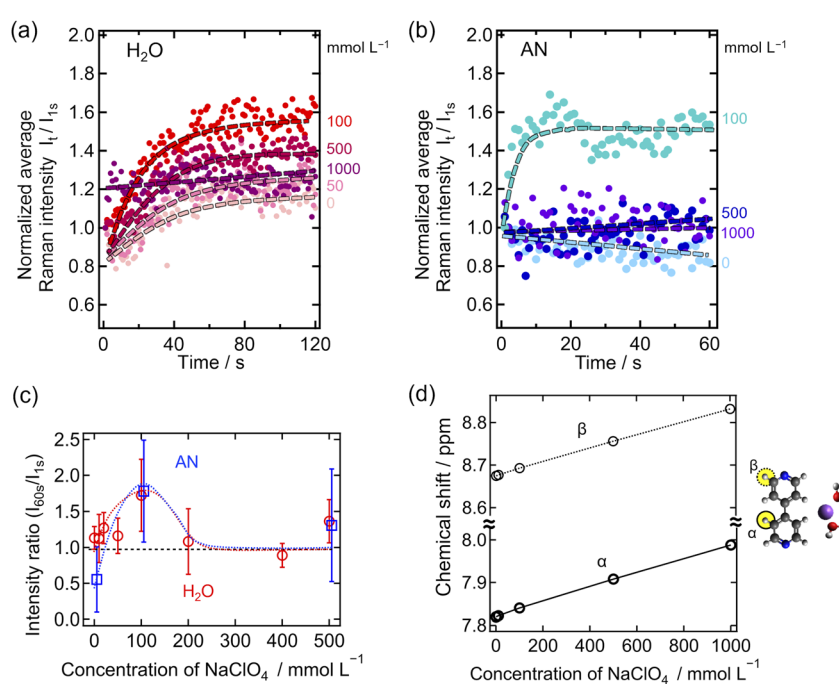


Fig. 3 Time dependent normalized average SERS intensities at  $1610\text{ cm}^{-1}$  are plotted various electrolyte concentrations of (a) 0 (beige), 50 (pink), 100 (red), 500 (purple), and 1000  $\text{mmol L}^{-1}$  (dark-purple) in  $\text{H}_2\text{O}$  or (b) 0 (light-blue), 100 (turquoise), 500 (blue), and 1000  $\text{mmol L}^{-1}$  (violet) in AN. The normalizations were conducted using more than 5 trials. Each dot is plotted from spectra obtained under  $140\text{ }\mu\text{W }\mu\text{m}^{-2}$  with 1 s exposure time. (c) The intensity ratios of the Raman intensity at 1 s to 60 s are plotted against electrolyte concentration from 0 to 500  $\text{mmol L}^{-1}$  in (a) and (b). (d) Chemical shifts of  $\alpha$ -hydrogen (solid line) and  $\beta$ -hydrogen (broken line) of 44bpy are measured by NMR in  $\text{D}_2\text{O}$  with different  $\text{NaClO}_4$  concentrations: 0, 10, 100, 500, and 1000  $\text{mmol L}^{-1}$ . The inset figure shows the scheme of the ionic interaction of 44bpy and  $\text{Na}^+$  cations.



<sup>1</sup>H NMR spectra of 44bpy in Fig. 3d shows that the amount of Na<sup>+</sup> binding to 44bpy causes a linear increase in the shift to a higher value as a function of electrolyte concentration. The trend of deshielding effects observed for 44bpy is evident for both hydrogen atoms at the  $\alpha$ - and  $\beta$ -positions, as shown in the inset figure (NMR spectra in Fig. SI-4).<sup>50</sup> The electrostatic interaction between Na<sup>+</sup> ions and aromatic rings, particularly those with electron-donating groups, is referred to as “cation– $\pi$  interaction”. This interaction results in a Gibbs energy change; for instance, a change of  $-88 \text{ kJ mol}^{-1}$  for Na<sup>+</sup> with benzene.<sup>56</sup> This stabilization energy is comparable to the Gibbs free-energy change associated with transferring 44bpy from solution to the adsorbed stand-up state (about  $-35 \text{ kJ mol}^{-1}$ ). It is an order of magnitude larger than the estimated van der Waals interaction between neighboring 44bpy molecules (up to  $-3.5 \text{ kJ mol}^{-1}$ ).<sup>31,51</sup> In addition, we estimated the Debye length ( $\lambda_D$ ) of a Na<sup>+</sup> cation under 100 mmol L<sup>-1</sup> conditions using the following equation.

$$\lambda_D = \left( \frac{\epsilon_r \epsilon_0 k_B T}{2N_A e^2 \sum c_i z_i^2} \right)^{1/2} \quad (2)$$

where  $\epsilon_r$  and  $\epsilon_0$  are the relative permittivity of the solvent and the vacuum ( $8.854 \times 10^{-12} \text{ F m}^{-1}$ ),  $k_B$  is the Boltzmann constant ( $1.381 \times 10^{-23} \text{ J K}^{-1}$ ),  $T$  is the solution temperature (298 K),  $N_A$  is Avogadro's number ( $6.022 \times 10^{23} \text{ mol}^{-1}$ ),  $e$  is the elementary charge ( $1.602 \times 10^{-19} \text{ C}$ ), and  $c_i$  and  $z_i$  represent the concentration and valency of ion species  $i$ , respectively.<sup>52–54</sup> From eqn (2), the estimated Debye length of the Na<sup>+</sup> cation is approximately 1 nm. This scale is comparable to the molecular dimensions of 44bpy (0.3–0.8 nm) and the intermolecular spacing within the stand-up adlayer (about 0.4 nm) observed by STM.<sup>55</sup> Because  $\lambda_D$  is inversely proportional to the square root of the ionic strength, it decreases with increasing electrolyte concentration. In water ( $\epsilon_r = 80.1$ ), the Debye lengths at 10, 100, and 1000 mmol L<sup>-1</sup> of NaClO<sub>4</sub> are approximately 3.1, 0.97, and 0.31 nm, respectively. In contrast, AN with  $\epsilon_r = 36.64$ , yields shorter Debye lengths under equivalent ionic conditions, approximately 2.1, 0.66, and 0.21 nm. Therefore, the efficient interaction between Na<sup>+</sup> and 44bpy, especially under 100 mmol L<sup>-1</sup> NaClO<sub>4</sub> conditions, is supported. The 44bpy molecule mainly acts as a Lewis base that interacts with cations or protons, while halide anions such as Cl<sup>-</sup> are unfavorable for forming  $\pi$ -interactions with the pyridyl ring ( $+8.4 \text{ kJ mol}^{-1}$ ).<sup>56</sup> In particular, at NaClO<sub>4</sub> concentrations below 1 mol L<sup>-1</sup>, it is difficult to attribute the observed behavior to direct anion– $\pi$  interaction. Here, ClO<sub>4</sub><sup>-</sup> mainly behaves as a weakly coordinating anion, similar to the role of water molecules as previously reported.<sup>57,58</sup> Our SERS measurements further show no distinct vibrational feature of ClO<sub>4</sub><sup>-</sup> at around 940 cm<sup>-1</sup> (spectral identification in Fig. SI-5).<sup>59</sup>

Moreover, because ClO<sub>4</sub><sup>-</sup> is a weak base, it may form hydrogen bonds with the C–H groups of the pyridyl skeleton, whereas Na<sup>+</sup> preferentially associates with the  $\pi$ -electron cloud. Consequently, both Na<sup>+</sup> and ClO<sub>4</sub><sup>-</sup> can contribute to the deshielding of the <sup>1</sup>H NMR peaks, although their individual effects cannot be clearly distinguished in this study. At higher NaClO<sub>4</sub> concentrations ( $>100 \text{ mmol L}^{-1}$ ), the ionic atmosphere

becomes sterically crowded and electrostatically screened, as the Debye length approaches the molecular dimensions of 44bpy (around 1 nm). Such crowding is likely to perturb the interfacial domain structure by enhancing steric and electrostatic repulsion, thereby disrupting molecular ordering. Considering the dimensions of the plasmonic field (approximately 500 nm<sup>3</sup>), it is essential to highlight that the current technique for plasmonic molecular manipulation facilitates the cooperative control of multiple molecular–ion pairs. This observation represents a foundational insight into the realm of plasmonic molecular manipulations, underscoring the potential for enhanced molecular interactions at the nanoscale.

### Formation of a distinct adsorbed phase driven by plasmonic retardation and ion-induced interactions beyond isothermal conditions

Finally, we summarized the condensed coverage of 44bpy in different solutions and electrolyte concentrations as shown in Fig. 4 (Table SI-3). The coverages were estimated from the density of the tightly packed stand-up 44bpy, which was determined to be  $6.9 \times 10^{-10} \text{ mol cm}^{-2}$ , as revealed by a previous STM study.<sup>55,60</sup> The experimental estimation coverage in H<sub>2</sub>O from Raman intensity, without the electrolyte, is  $8.0 \times 10^{-10} \text{ mol cm}^{-2}$ , assuming the initial coverage of 100%. This discrepancy implies that the plasmon local electric field not only facilitates molecular condensation in the hotspot by slowing diffusion velocity but also promotes a tightly packed arrangement through the entire domain structure beyond the thermal isotherm as estimated from electrochemical measurements.<sup>31,53,51</sup> On the other hand, the estimated coverages after illumination in other solutions without electrolytes show lower values, indicating a more spatially dispersed distribution due to a reduced adsorption amount. It should be noted that the difference in coverage primarily arises from the amount of adsorption, which correlates with the variation in the Gibbs free energy change between the solvated and adsorbed states, an essential aspect of interfacial phenomena. This is supported by the fact that their intensities vary depending on the solvent from initial illumination, although the adsorbed 44bpy molecules are all assigned as standing upright based on the spectral

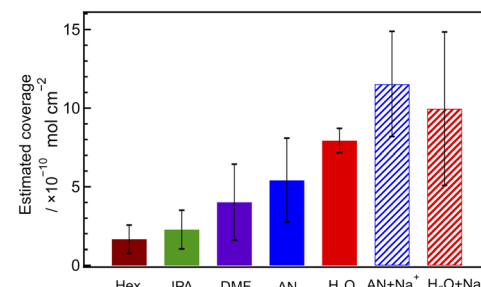
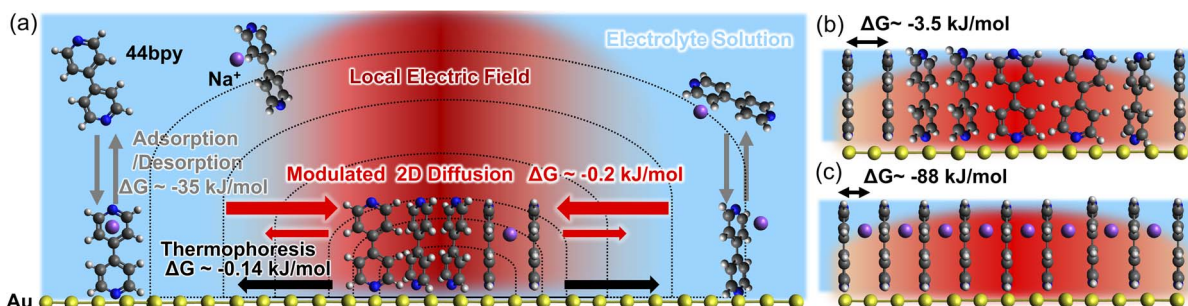


Fig. 4 Estimated coverages from the SERS intensity after 60 s illumination are shown as brown, green, purple, blue, and red color bars for Hex, IPA, DMF, AN, and H<sub>2</sub>O, respectively. In the 100 mM NaClO<sub>4</sub> solution H<sub>2</sub>O (blue) and AN (red) are shown as shaded bars. Black lines correspond to deviations of those estimated coverages.





**Fig. 5** Schematic illustration of plasmon-driven optical condensation of 44bpy molecules at the hotspot between Au nanoprisms with electrolyte ( $\text{NaClO}_4$ ); (a) Arrows indicate molecular fluxes arising from adsorption/desorption equilibrium (grey), thermophoretic migration induced by plasmonic heating (black), and optically modulated two-dimensional diffusion along the electric field gradient (red). Black dots represent thermal contours generated by localized surface plasmon resonance. (b) Schematic illustration of a loosely packed 44bpy domain stabilized by van der Waals interactions between 44bpy molecules in a planar configuration. (c) Upon addition of an appropriate concentration of electrolyte, surface packing is enhanced via cation- $\pi$  interactions, resulting in a distinct phase with increased molecular density and improved lateral ordering. The values of Gibbs free energy change are taken from the main text.

shapes in  $\text{H}_2\text{O}$ , AN, IPA, and Hex, as discussed in Fig. 1. Upon introduction of the electrolyte, the displacement before and after illumination increased to  $10 \times 10^{-10} \text{ mol cm}^{-2}$  for  $\text{H}_2\text{O}$ , indicating that the static interactions of ions in the  $100 \text{ mmol L}^{-1}$  electrolyte strongly promote molecular packing or the organization of larger domains. In the case of AN, the addition of  $100 \text{ mmol L}^{-1}$  electrolyte significantly modulated the initial coverage and enhanced the intensity under light illumination, resulting in the values of  $8.6$  and  $12 \times 10^{-10} \text{ mol cm}^{-2}$ , respectively. This might be due to the lower volume concentration of AN compared to  $\text{H}_2\text{O}$ , with  $\text{H}_2\text{O}$  at  $55.3 \text{ mol L}^{-1}$  and AN at  $19.0 \text{ mol L}^{-1}$ , which effectively affects the cation- $\pi$  interaction of 44bpy and  $\text{Na}^+$  at the interface.

From these observations, the overall mechanism of plasmon-induced molecular condensation is proposed as illustrated in Fig. 5a, which shows the dynamic interfacial behavior of 44bpy molecules under illumination. Continuous adsorption and desorption occur between the bulk solution and the Au surface. Localized heating generates thermophoretic flows that drive molecules outward from the hotspot. Simultaneously, optical field gradients enhance inward 2D diffusion toward the hotspot center and suppress outward migration, resulting in an asymmetric lateral diffusion profile. This nonequilibrium molecular transport leads to localized accumulations, particularly in solvents with lower thermal diffusion such as  $\text{H}_2\text{O}$ . Otherwise, in solvents with higher thermal diffusivity, the effective thermal potential of 44bpy, exceeding  $-0.35 \text{ kJ mol}^{-1}$ , overcomes the optical potential ( $-0.20 \text{ kJ mol}^{-1}$ ), thereby preventing accumulations at the hotspot. Fig. 5b depicts the formation of packed molecular domains driven by plasmon-induced optical force defined by electric field gradients. Upon addition of electrolytes, Fig. 5c shows that cation- $\pi$  interactions between  $\text{Na}^+$  and 44bpy promote lateral intermolecular attraction, leading to more compact packing and increased surface coverage up to  $12 \times 10^{-10} \text{ mol cm}^{-2}$  in the presence of  $100 \text{ mmol L}^{-1}$   $\text{NaClO}_4$  in  $\text{H}_2\text{O}$ . This organized domain surpasses the level of condensation achieved under optical fields alone or thermal equilibrium without illumination. Together, these schematics demonstrate

that interfacial molecular condensation is not governed solely by optical force. Instead, it emerges from a complex interplay among optical forces, thermophoresis, solvation dynamics, and static ion-molecule interactions. The result is the formation of a distinct, non-isothermal condensed molecular phase at interfaces.

## Conclusions

We have successfully achieved plasmonic molecular condensations under various solution conditions at room temperature. This study identifies key factors influencing plasmonic molecular trapping, including adsorption equilibrium determined by solvation, thermophoresis, 2D diffusion retardation, and electrostatic interaction mediated by ions. In the present system,  $\text{Na}^+$  is expected to bridge the 44bpy molecules, thereby stabilizing their adsorption at the interface and counteracting the drawbacks of thermal diffusion in the AN solution. This insight provides a much more precise direction for controlling electrochemistry or interfacial science, especially combined with nanostructure design. In addition, as the side effect of optical perturbation force, it is suggested that there is additional condensation or formation of higher packed states up to  $12 \times 10^{-10} \text{ mol cm}^{-2}$  under the present condition beyond the thermodynamic equilibrium value of  $6.9 \times 10^{-10} \text{ mol cm}^{-2}$ .<sup>55,60</sup> While our study demonstrates the formation of nonequilibrium molecular condensates under plasmonic excitation, we emphasize that several limitations are remained. The relaxation dynamics after stopping illumination suggest partial but not complete recovery to the initial state, reflecting the persistence of intermolecular interactions observed in present experiments and the previous report.<sup>11</sup> In addition, our estimation of thermal diffusion velocity was based on bulk solvent parameters, which may not fully capture the interfacial behavior at metal-solution interfaces. These limitations underscore the need for future investigations that integrate molecular-scale thermal transport and microfluidic dynamics at solid-liquid interfaces, where plasmonic devices will also play a crucial role in controlling and probing molecular dynamics. Recent studies



indicate that optical pressure or electric fields can induce a specific structure in trapped molecules by promoting interactions between them.<sup>44,61</sup> Importantly, with the presence of ions, the enhanced intermolecular forces and the plasmon-induced electric field cooperatively drive the system into a new steady state of adsorption and desorption that differs from that under the conventional thermal equilibrium. This cooperative effect enables the selective condensation and separation of target molecules in solution that could not be achieved by either chemical or optical means. While our present analysis referenced the Temkin isotherm for estimating initial coverage, the observed nonequilibrium steady states under illumination highlight the need for future theoretical frameworks that incorporate optical forces, dissipative dynamics, and thermophoretic transport beyond conventional equilibrium adsorption models. Consequently, our findings contribute not only to provide a deeper understanding of light-induced chemical interactions but also to open new avenues for molecular manipulation, interfacial control, and plasmonic nanoscience.

## Methods

### Sample solution preparation

4,4'-Bipyridine was chosen as the trapping target molecule, which was known to be physically adsorbed on the Au surface as a single monolayer in solution.<sup>31-33</sup> All chemicals were purchased from FUJIFILM Wako Pure Chemical Corp., Japan. The powder of 1 mM 44bpy (97.0%) was dissolved in various solvents, ultrapure H<sub>2</sub>O (>18.2 MΩ grade; Milli-Q Advantage, Merck KGaA), *N,N'*-dimethylformamide (99.5%), acetonitrile (99.5%), isopropanol (99.7%), or *n*-hexane (96.0%). All solvents were used without any purification. The solutions were stored in a temperature- and humidity-controlled darkroom, where the Raman measurements were also performed. Before each measurement, approximately 5 mL of solution was immediately transferred into the cell, and each spectrum was acquired within a few minutes.

### Fabrication of the plasmon-active Au substrate

The plasmon-active Au nanoprisms were prepared by the template method as in our previous reports.<sup>26,34,35</sup> A 400 μL solution of polystyrene bead (Polyscience, Inc., 200 nm diameter) was centrifuged to remove the supernatant. Then, 100 μL of Milli-Q water and 150 μL ethanol were added. After preparing polystyrene bead solutions, the self-assembled monolayer of polystyrene beads was prepared on the surface of ITO glass. Then 30 nm of Au was deposited onto the polystyrene bead monolayer by electron beam deposition for each ±10° tilt with a crystal rate thickness monitor (ULVAC, Inc.). After the deposition, all the polystyrene beads were removed by sonication in tetrahydrofuran (FUJIFILM Wako Pure Chemical Corporation) and Milli-Q water. Overall, the fabricated Au structure features an array of nanoprism dimers with triangular shapes approximately 60 nm in size.

### Optical setup for Raman measurement

The polarized Raman measurement is conducted under excitation with 785 nm continuous laser. The detailed setup is provided in our previous report.<sup>11,38</sup> The laser power at the sample position was set to 1.0–2.0 mW through a water immersion objective lens (×100, N. A. = 1.00, W. D. = 1.5 mm, OLYMPUS). Since the laser spot size at the ITO glass/liquid interface reaches up to 3 μm, the incident laser intensities ( $I_{ex}$ ) were estimated as 140/280 μW μm<sup>-2</sup>. All spectra were acquired with an acquisition time of 1 s and a number of acquisitions of 1–120 during continuous laser exposure. The substrate was at the bottom of the solution in a glass container.

## Author contributions

K. M. and H. M. designed the research; N. O. conducted all experiments and data analyses; N. O., H. M., and K. M. interpreted the results and prepared this manuscript.

## Conflicts of interest

There are no conflicts to declare.

## Data availability

All data supporting the findings of this study are available within the article and its Supplementary Information file. The raw data that support the findings of this study are available from the corresponding author upon reasonable request.

All data supporting the findings of this study are available within the article and its supplementary information (SI). Supplementary information: AFM images and optical properties of a nanoprism array substrate, representative spectra of 44bpy in various solvents, correlation plot of each vibrational peak for analyzing the orientation, thermodynamic analysis of 44bpy diffusion in each organic solvent, surface coverage estimation of 44bpy in different solutions under illumination, NMR measurements of dissolved 44bpy with added NaClO<sub>4</sub>, and representative time-series spectra with added NaClO<sub>4</sub> (PDF). See DOI: <https://doi.org/10.1039/d5sc05604g>.

## Acknowledgements

We appreciate the discussion with Hajime Ishihara (Osaka University) and Keiji Sasaki (Hokkaido University). This work was partially supported by JSPS KAKENHI Grants-in-Aid for Scientific Research (JP18K14309 and JP18H05205) and Grants-in-Aid for JSPS Fellows (JP20J20967) from the Ministry of Education, Culture, Sports, Science, and Technology of Japan. We especially appreciate a lot of support by Scientific Research on Innovative Areas “Nano-Material Optical-Manipulation” (JP16H06506). Support of the JST-Mirai Program (JPMJMI21EB), the Frontier Photonic Sciences Project of National Institutes of Natural Sciences (NINS; 01213010), and the Photo-excitonix Project at Hokkaido University are also acknowledged.



## References

- 1 A. Ashkin, J. M. Dziedzic, J. E. Bjorkholm and S. Chu, *Opt. Lett.*, 1986, **11**, 288–290.
- 2 D. G. Grier, *Nature*, 2003, **424**, 810–816.
- 3 O. M. Maragò, P. H. Jones, P. G. Gucciardi, G. Volpe and A. C. Ferrari, *Nat. Nanotechnol.*, 2013, **8**, 807–819.
- 4 K. Dholakia, P. Reece and M. Gu, *Chem. Soc. Rev.*, 2008, **37**, 42–55.
- 5 H. Misawa, M. Koshioka, K. Sasaki, N. Kitamura and H. Masuhara, *J. Appl. Phys.*, 1991, **70**, 3829–3836.
- 6 S. F. Wang, T. Kudo, K. I. Yuyama, T. Sugiyama and H. Masuhara, *Langmuir*, 2016, **32**, 12488–12496.
- 7 R. Zhu, T. Avsievich, A. Popov and I. Meglinski, *Cells*, 2020, **9**, 545.
- 8 M. L. Juan, M. Righini and R. Quidant, *Nat. Photonics*, 2011, **5**, 349–356.
- 9 C. Bradač, *Adv. Opt. Mater.*, 2018, **6**, 1800005.
- 10 H. Xu and M. Käll, *Phys. Rev. Lett.*, 2002, **89**, 246802.
- 11 N. Oyamada, H. Minamimoto and K. Murakoshi, *J. Am. Chem. Soc.*, 2022, **144**, 2755–2764.
- 12 M. L. Juan, R. Gordon, Y. Pang, F. Eftekhari and R. Quidant, *Nat. Phys.*, 2009, **5**, 915–919.
- 13 D. O. Sigle, S. Kasera, L. O. Herrmann, A. Palma, B. De Nijs, F. Benz, S. Mahajan, J. J. Baumberg and O. A. Scherman, *J. Phys. Chem. Lett.*, 2016, **7**, 704–710.
- 14 E. A. Sprague-Klein, M. O. McAnally, D. V. Zhdanov, A. B. Zrimsek, V. A. Apkarian, T. Seideman, G. C. Schatz and R. P. Van Duyne, *J. Am. Chem. Soc.*, 2017, **139**, 15212–15221.
- 15 H. Niinomi, T. Sugiyama, M. Tagawa, M. Maruyama, T. Ujihara, T. Omatsu and Y. Mori, *Cryst. Growth Des.*, 2017, **17**, 809–818.
- 16 M. L. Brongersma, N. J. Halas and P. Nordlander, *Nat. Nanotechnol.*, 2015, **10**, 25–34.
- 17 Y. Nishijima, K. Ueno, Y. Kotake, K. Murakoshi, H. Inoue and H. Misawa, *J. Phys. Chem. Lett.*, 2012, **3**, 1248–1252.
- 18 S. Linic, U. Aslam, C. Boerigter and M. Morabito, *Nat. Mater.*, 2015, **14**, 567–576.
- 19 W. Chen, P. Roelli, H. Hu, S. Verlekar, S. P. Amirtharaj, A. I. Barreda, T. J. Kippenberg, M. Kovalina, E. Verhagen, A. Martínez and C. Galland, *Science*, 2021, **374**, 1264–1267.
- 20 H. Nabika, A. Sasaki, B. Takimoto, Y. Sawai, S. He and K. Murakoshi, *J. Am. Chem. Soc.*, 2005, **127**, 16786–16787.
- 21 Y. Zhang, C. Min, X. Dou, X. Wang, H. P. Urbach, M. G. Somekh and X. Yuan, *Light:Sci. Appl.*, 2021, **10**, 59.
- 22 M. Braibanti, D. Vigolo and R. Piazza, *Phys. Rev. Lett.*, 2008, **100**, 108303.
- 23 S. Duhr and D. Braun, *Proc. Natl. Acad. Sci. U. S. A.*, 2006, **103**, 19678–19682.
- 24 T. Shoji and Y. Tsuboi, *J. Phys. Chem. Lett.*, 2014, **5**, 2957–2967.
- 25 A. Zehtabi-Oskui, J. G. Bergeron and R. Gordon, *Sci. Rep.*, 2012, **2**, 966.
- 26 N. Oyamada, H. Minamimoto, Y. Wakisaka and K. Murakoshi, *Chem. Lett.*, 2019, **48**, 820–823.
- 27 C. Kojima, A. Noguchi, T. Nagai, K. Yuyama, S. Fujii, K. Ueno, N. Oyamada, K. Murakoshi, T. Shoji and Y. Tsuboi, *ACS Omega*, 2022, **7**, 13120–13127.
- 28 E. C. Le Ru and P. G. Etchegoin, *Annu. Rev. Phys. Chem.*, 2012, **63**, 65–87.
- 29 R. Zhang, Y. Zhang, Z. C. Dong, S. Jiang, C. Zhang, L. G. Chen, L. Zhang, Y. Liao, J. Aizpurua, Y. Luo, J. L. Yang and J. G. Hou, *Nature*, 2013, **498**, 82–86.
- 30 G. Chirico, C. Fumagalli and G. Baldini, *J. Phys. Chem. B*, 2002, **106**, 2508–2519.
- 31 K. Uosaki, H. Allen and O. Hill, *J. Electroanal. Chem. Interfacial Electrochem.*, 1981, **122**, 321–326.
- 32 Y. Zhang, R. Zhang, S. Jiang, Y. Zhang and Z.-C. Dong, *ChemPhysChem*, 2019, **20**, 37–41.
- 33 D. Yang, D. Bizzotto, J. Lipkowski, B. Pettinger and S. Mirwald, *J. Phys. Chem.*, 1994, **98**, 7083–7089.
- 34 S. Oikawa, H. Minamimoto and K. Murakoshi, *J. Phys. Chem. C*, 2022, **126**, 1188–1195.
- 35 C. L. Haynes and R. P. Van Duyne, *J. Phys. Chem. B*, 2001, **105**, 5599–5611.
- 36 S. K. Ghosh, S. Nath, S. Kundu, K. Esumi and T. Pal, *J. Phys. Chem. B*, 2004, **108**, 13963–13971.
- 37 M. Suzuki, Y. Niidome and S. Yamada, *Thin Solid Films*, 2006, **496**, 740–747.
- 38 N. Oyamada, H. Minamimoto and K. Murakoshi, *J. Phys. Chem. C*, 2019, **123**, 24740–24745.
- 39 M. Futamata, Y. Maruyama and M. Ishikawa, *Vib. Spectrosc.*, 2004, **35**, 121–129.
- 40 T. Tsuji, K. Doi and S. Kawano, *J. Photochem. Photobiol. C*, 2022, **52**, 100533.
- 41 Q. Jiang, B. Rogez, J. B. Claude, G. Baffou and J. Wenger, *Nano Lett.*, 2020, **20**, 8811–8817.
- 42 J. D. Tirado, D. Acevedo, R. L. Bretz and H. D. Abruña, *Langmuir*, 1994, **10**, 1971–1979.
- 43 N. S. Gould, S. Li, H. J. Cho, H. Landfield, S. Caratzoulas, D. Vlachos, P. Bai and B. Xu, *Nat. Commun.*, 2020, **11**, 1–13.
- 44 S. Wang, J. Lin, F. Ishiwari, T. Fukushima, H. Masuhara and T. Sugiyama, *Angew. Chem.*, 2020, **132**, 7129–7134.
- 45 D. Shin, J. Hwang and W. Jhe, *Nat. Commun.*, 2019, **10**, 1–8.
- 46 T. Fukushima, S. Yoshimitsu and K. Murakoshi, *J. Am. Chem. Soc.*, 2022, **144**, 12177–12183.
- 47 X. Chen, Y. Chen, M. Yan and M. Qiu, *ACS Nano*, 2012, **6**, 2550–2557.
- 48 A. Thomas, L. Lethuillier-Karl, K. Nagarajan, R. M. A. Vergauwe, J. George, T. Chervy, A. Shalabney, E. Devaux, C. Genet, J. Moran and T. W. Ebbesen, *Science*, 2019, **363**, 615–619.
- 49 H. Minamimoto, R. Zhou, T. Fukushima and K. Murakoshi, *Acc. Chem. Res.*, 2022, **55**, 809–818.
- 50 M. Bielejewski, A. Rachocki, J. Kaszyńska and J. Tritt-Goc, *Phys. Chem. Chem. Phys.*, 2018, **20**, 5803–5817.
- 51 F. Cunha, N. J. Tao, X. W. Wang, Q. Jin, B. Duong and J. D’Agnese, *Langmuir*, 1996, **12**, 6410–6418.
- 52 P. Debye and E. Hückel, *Phys. Z.*, 1923, **24**, 185–206.
- 53 S. Prakash and J. Yeom, *Nanofluidics and microfluidics: systems and applications*, William Andrew, 2014.



54 *CRC Handbook of Chemistry and Physics*, ed. W. M. Haynes, CRC Press, Boca Raton, 95th edn, 2014.

55 T. Wandlowski, K. Ataka and D. Mayer, *Langmuir*, 2002, **18**, 4331–4341.

56 A. Frontera, P. Gamez, M. Mascal, T. J. Mooibroek and J. Reedijk, *Angew. Chem., Int. Ed.*, 2011, **50**, 9564–9583.

57 H. Zhang, D. Raciti and A. S. Hall, *Nat. Chem.*, 2025, **17**, 1161–1168.

58 C.-Y. Li, M. Chen, S. Liu, X. Lu, J. Meng, J. Yan, H. D. Abruña, G. Feng and T. Lian, *Nat. Commun.*, 2022, **13**, 5330.

59 M. H. Lee, S. J. Kim, D. Chang, J. Kim, S. Moon, K. Oh, K.-Y. Park, W. M. Seong, H. Park, G. Kwon, B. Lee and K. Kang, *Mater. Today*, 2019, **29**, 26–36.

60 D. Mayer, T. Dretschkow, K. Ataka and T. Wandlowski, *J. Electroanal. Chem.*, 2002, **524**–525, 20–35.

61 J. S. Lu, H. Y. Wang, T. Kudo and H. Masuhara, *J. Phys. Chem. Lett.*, 2020, **11**, 6057–6062.

